Developing a Filtering Algorithm for Partial Discharge Location Approximation Using the Emitted Electromagnetic Signals of Corona Discharges

Máté Szirtes, Richárd Cselkó, and István Berta

***Abstract*—The aim of this article is to create a novel filtering algorithm for the emitted electromagnetic signals of corona discharges, using the special time-domain features of the continuous wavelet transform. The first part of this article therefore focuses on the time-domain examination of these signals to find characteristic features that are compatible with the wavelet transform. The second part of this article utilizes these features to create and validate the filtering algorithm. This is an important step toward creating an accurate three-dimensional partial discharge location approximation system that could contribute to preventing and finding partial-discharge-related faults. In the presented research, needle–plane corona discharge sources with different geometries are tested at both ac and dc voltages.**

***Index Terms*—Corona, filtering, partial discharge, rise time, time of arrival estimation, wavelet transform.**

I. Introduction

PARTIAL discharges (PDs) occurring in air can be linked to the onset of degradation in various fields of electrical and electronics engineering [1]–[3]. Their presence can be the sign of a forthcoming fault in various high-voltage equipment or it can indicate an unwanted level of electrostatic charge accumulation on electrodes with a small radius of curvature. The emitted electromagnetic disturbances of PDs can cause interferences in wireless communication [4], [5], but they also provide a promising opportunity to locate the discharge source and fix the underlying problem [6].

The location approximation of PDs is achievable by antenna measurements and proper signal processing [7], [8]. The most important part of this processing is the noise filtering of the measured signals [9]–[11], because it directly affects the positioning accuracy of the measuring system. To adopt the noise filtering to the discharge phenomenon, it is necessary to perform a comprehensive examination on the characteristics of the emitted signals [12], [13]. This article presents the time-domain examination of emitted corona discharge signals and the development steps of a wavelet-transform-based novel filtering algorithm. This is a key step for the development of a corona discharge positioning system that could be used in various fields of industry applications, where the presence of corona discharges is unwanted.

Manuscript received May 13, 2020; accepted October 17, 2020. Date of publication November 17, 2020; date of current version December 31, 2020. Paper 2020-EPC-0832, presented at the 2019 IEEE Industry Applications Society Annual Meeting, Baltimore, MD USA, Sep. 29–Oct. 3, and approved for publication in the IEEE Transactions on Industry Applications by the Electrostatic Processes Committee of the IEEE Industry Applications Society. *(Corresponding author: Richárd Cselkó.)*

The authors are with the Group of High Voltage Technology and Equipment, Budapest University of Technology and Economics, Budapest 1111, Hungary (e-mail: mate.szirtes@gmail.com; cselko.richard@vet.bme.hu; berta.istvan@vet.bme.hu).

Color versions of one or more of the figures in this article are available at https://doi.org/10.1109/TIA.2020.3038627.

Digital Object Identifier 10.1109/TIA.2020.3038627

II. Examination of Corona Discharges

A. Measurement Methodology

In the presented research phase, various needle–plane corona discharge geometries were examined using a 500-MHz digital sampling oscilloscope (DSO) with 4-GSa/s sampling rate and a gigahertz transverse electromagnetic cell that can be used in the 9 kHz to 5 GHz frequency band. The cell provides a noise-free measuring environment and directs the electromagnetic signals toward the connecting 50-Ω coaxial cable of the oscilloscope, making it possible to directly examine these signals without the use of an antenna. These measurements make it possible to identify the main time-domain characteristics of the emitted corona discharge pulses, by examining these signals for different electrode geometries, electrode distances, voltage levels, and frequencies (50 Hz ac and dc). By varying all these parameters, the aim is to find the basic characteristic features of the emitted corona signals and see how they are affected by these parameters. Fig. 1 shows the schematic of the measuring arrangement.

To examine the effect of inhomogeneity on the emitted signals of corona discharges, four different needle–plane arrangements were used during the measurements. The inhomogeneity of each arrangement's electric field distribution is reflected by the ratio of the electrode distance and the curvature diameter of the needle tip. In a homogeneous plane–plane arrangement, this inhomogeneity ratio would be zero. The main geometric parameters and the inhomogeneity ratios of the four arrangements are presented in Table I.

Each arrangement was tested for five different levels of positive and negative voltages using both 50-Hz ac and dc sources,

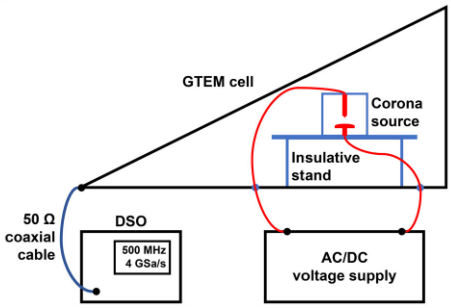

Fig. 1. Schematic of the used measuring arrangement.

TABLE I
SIZE PARAMETERS OF THE USED ELECTRODE ARRANGEMENTS

Arrangement name	Needle tip diameter (d)	Electrode distance (D)	Inhomogeneity ratio (D/d)
Blunt-10	1.2 mm	10 mm	8.3
Blunt-15	1.2 mm	15 mm	12.5
Sharp-10	0.3 mm	10 mm	33.3
Sharp-15	0.3 mm	15 mm	50

as shown in Table II. In the case of the ac source, the positive and negative polarities refer to the inspected half-cycle of the sinusoidal testing voltage. The voltage polarity is defined positive, when the needle is on positive potential compared with the plane electrode.

The lower boundary of the chosen ac and dc voltages is the corona inception voltage, above which the discharge pulses are captured at a constant rate. The upper ac boundary is the breakdown voltage of the arrangement, where the measured PD turns into an electric arc between the two electrodes, whereas the upper dc limit is defined by the voltage where the corona turns into a glow discharge. During the occurrence of the glow discharge, individual emitted pulses cannot be measured, because of the continuous nature of this phenomenon. At higher voltages, the glow discharge is followed by a breakdown in the electrode gap.

This difference between the upper boundaries of the ac and dc testing voltages is due to their different shapes. Although the glow discharges are already present near the peaks of the sine wave at higher ac voltages, the corona discharges are still present at the lower voltages around the zero-crossing, and thus the discharge pulses can be captured until breakdown occurs.

It must also be noted that these lower and upper voltage boundaries are different for each arrangement. In the dc case, these boundaries properly reflect the effect of polarity on the different discharge phenomena. Table II shows that the corona inception occurs at slightly lower voltage values if the polarity is negative, whereas the glow discharge occurs earlier when the dc voltage is positive. In the case of the ac voltage tests, the inception of the positive and negative corona pulses happens at approximately same rms value. The upper ac limit is also the same, because the first occurring positive breakdown prevents us from measuring further negative corona pulses above that voltage value.

B. Applicability of the Wavelet Transform

As it was mentioned before, the aim of this research study is to use the obtained characteristic corona features to develop a novel filtering algorithm for a corona discharge location approximation system. For the accuracy of the positioning process, the determined arrival time differences between the measured noisy signals [time difference of arrival (TDOA)] must be sufficiently accurate. This means that the aim of the filtering process is to accurately measure the arrival time values (time of arrival - TOA) of the captured emitted signals. With this in mind, the examination must be focused on the beginning of the captured signal. In the representative time-domain voltage signal examples shown in Fig. 2, there is a steep pulse at the beginning of each measured signal, which is followed by a longer, oscillating transient with higher amplitude. This low-frequency transient is the response of the whole measuring system to the first voltage pulse, which is the original corona signal [14].

The downside of the more traditional frequency-domain examination is that it is aimed to be used for periodic signals, as the observed signal is decomposed to a continuous range of different frequency sine waves. By using a Fourier-transform-based bandpass filter, the original time-domain characteristics of the corona pulse are not preserved, as the resulting signal will have a dominant sinusoidal component, which can distort the actual TOA measurement of the signal.

To solve this problem, not only the frequency content but also the time-domain waveform of the signal should be taken into consideration during noise filtering. The wavelet-transform-based noise filtering methods successfully combine these two elements, as they decompose the observed signal to different frequency wavelet functions with specific waveforms [15], [16]. These wavelet functions have an aperiodic behavior, similar to the emitted corona discharge signals, and the used wavelet type can be freely chosen according to the shape of the corona signal.

The wavelet transform is based on the wavelet function $\Psi(t)$, also known as the mother wavelet. This function is a short time-domain oscillation and has three well-defined mathematical features [17]. The first feature is that it has a mean value of 0, as shown in (1), accordingly the oscillation is evenly above and below this level. The second feature is that its total signal energy equals to 1, as describe in (2). The third feature of the wavelet function is that it is localized in time, meaning that outside of a finite time window, its value is always 0, as the investigated wavelet functions of Fig. 5 show

$$\int_{-\infty}^{\infty} \Psi(t)\, dt = 0 \tag{1}$$

$$\int_{-\infty}^{\infty} |\Psi(t)|^2 dt = 1. \tag{2}$$

The mother wavelet works as a special bandpass filter in the frequency domain because of its oscillating nature and its zero mean value. The frequency-domain features of this bandpass filter can be specified by the time-domain modification of the mother wavelet, using the parameters a and b, as shown in the

TABLE II
TESTING VOLTAGES OF THE USED ELECTRODE ARRANGEMENTS

Voltage type and polarity	Electrode arrangement	Lower voltage boundary (corona inception)	Testing voltage 1	Testing voltage 2	Testing voltage 3	Testing voltage 4	Testing voltage 5	Upper voltage boundary (AC: breakdown, DC: glow discharge)
AC - Negative [kV_{RMS}]	Blunt-10	6.70	6.80	7.05	7.30	7.55	7.80	7.90
	Blunt-15	8.40	9.00	9.50	10.00	10.50	11.00	12.40
	Sharp-10	4.70	5.00	6.00	7.00	8.00	9.00	9.60
	Sharp-15	4.80	5.00	7.00	9.00	11.00	13.00	14.40
AC - Positive [kV_{RMS}]	Blunt-10	6.70	6.80	7.05	7.30	7.55	7.80	7.90
	Blunt-15	8.40	9.00	9.50	10.00	10.50	11.00	13.00
	Sharp-10	4.70	5.00	6.00	7.00	8.00	9.00	9.60
	Sharp-15	4.80	5.00	7.00	9.00	11.00	13.00	14.40
DC - Negative [kV]	Blunt-10	-8.00	-8.50	-9.00	-9.50	-10.00	-10.50	-11.00
	Blunt-15	-9.50	-10.50	-11.50	-12.50	-13.50	-14.50	-15.50
	Sharp-10	-4.60	-4.70	-5.20	-5.70	-6.20	-6.70	-7.00
	Sharp-15	-6.50	-9.80	-10.05	-10.30	-10.55	-10.80	-14.30
DC - Positive [kV]	Blunt-10	8.60	8.80	9.05	9.30	9.55	9.80	10.00
	Blunt-15	9.50	9.80	10.05	10.30	10.55	10.80	11.10
	Sharp-10	5.30	5.30	5.40	5.50	5.60	5.70	5.80
	Sharp-15	6.80	6.85	6.95	7.05	7.15	7.25	7.40

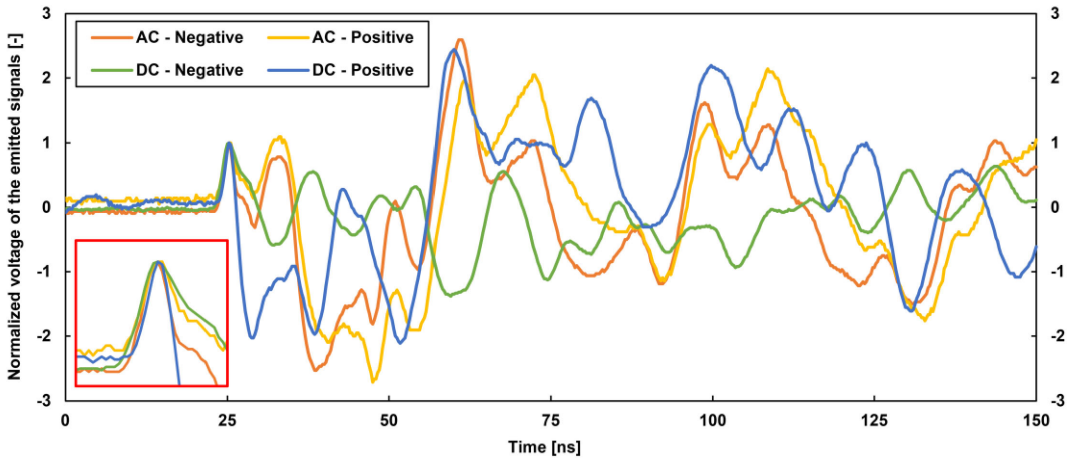

Fig. 2. Representative emitted waveforms of the four examined types of corona discharges.

following equation [18]:

$$\Psi_{a,b}(t) = \frac{1}{\sqrt{a}} \cdot \Psi\left(\frac{t-b}{a}\right). \tag{3}$$

The dimensionless parameter a is called the *scale* parameter, and it makes it possible to stretch the wavelet function along the time axis, modifying the center frequency of the mother bandpass filter by a multiplier of $1/a$. The time dimension parameter b is called the *shift* parameter, and it makes it possible to slide the wavelet function along the time axis, which is needed for the filtering process. This process is described in (4), where the two-dimensional (2-D) values of the continuous wavelet transform (CWT) for the time-domain signal $x(t)$ are presented [18]. In this 2-D space of wavelet coefficients, the resulting bandpass filtered signals are given for each value of the a parameter, where the values of b form the time axis of the filtered signal, and the center frequency of the filtering is proportional to $1/a$

$$W_x(a,b) = \int_{-\infty}^{\infty} \{x(t) \cdot \Psi_{a,b}(t)\}\, dt. \tag{4}$$

There are several types of wavelets, having different time- and frequency-domain features, making them able to filter specific types of signals. The so-called wavelet families consist of different wavelets that share some basic attributes. The parts of a wavelet family are called the different orders of that family. The various time- and frequency-domain features of each wavelet type make it possible to accurately define a CWT-based bandpass filter using the time-domain characteristics of the investigated emitted corona signals.

C. Time-Domain Examination

The motivation of the time-domain examination comes from the representative signals shown in Fig. 2, where the waveforms were normalized to their first peak to visually compare their characteristic features. These normalized waveforms show that the rising slope of the first pulse shows significant similarities regardless of the signal being ac, dc, positive, or negative.

The most important time-domain parameter of the first corona pulse is its rise time that can be calculated, as shown in Fig. 3. If this value is constant during the various measurements, the

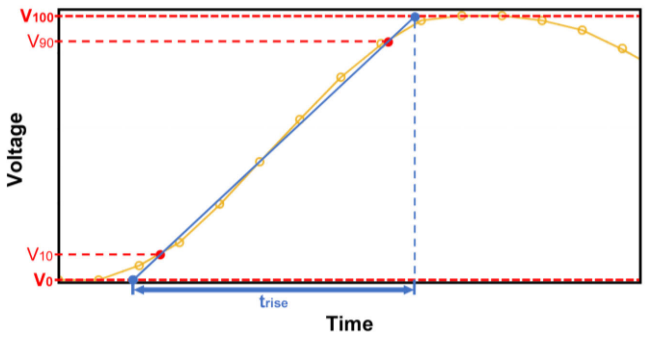

Fig. 3. Rise time calculation method of the observed corona pulse.

horizontal scaling of the used wavelet can be set accordingly to have the same rise time value at its dominant pulse. This way, the wavelet-based filtering process will successfully highlight the first corona pulse without distorting its arrival time value.

For the time-domain examination, the rise time of the first pulse was determined for every testing voltage presented in Table II using the calculating method shown in Fig. 3. This method linearizes the slope of the observed pulse by connecting its 10% (V_{10}) and 90% (V_{90}) values by a straight line. The rise time (t_{rise}) is defined by the time difference between this line crossing the minimum (V_0) and maximum (V_{100}) values.

The resulting rise time values did not show any consistent dependence of the five different voltage levels. Accordingly, for the final evaluation, the average of these five time values was calculated and compared, as shown in the results in Fig. 4. The indicated rise times are the averaged values, whereas the error bars show the highest and lowest individual values of the averaged five measurements for each arrangement.

The results in Fig. 4 show that the rise time values are slightly higher in case of the dc measurements. It can also be seen that average rise times show low deviation both from each other and from all of the individual measured values, which is in accordance with the visual expectations from the signals shown in Fig. 2. This low deviation of the average results makes the resulting rise time values applicable for setting the parameters of the wavelet filter. By setting the horizontal *scale* parameter of the chosen wavelet accordingly, the rise time of its dominant pulse can be set to the average value of approximately 1.63 ns to properly match the observed corona pulse.

It must also be noted that this similarity in the rise times is a valid result and it is not caused by the limited bandwidth of the measuring system. According to the manufacturer of the used DSO, the $t_r = 0.35/BW$ equation can be used as a general rule of thumb to define the shortest measurable t_r rise time in the case of a given BW analog bandwidth [19]. Therefore, in our case, the 500-MHz analog bandwidth of the DSO makes it possible to measure rise times down to 0.7 ns, which is less than half of our measured average rise time of 1.63 ns.

III. Development of the Filtering Algorithm

A. Parameterization of the Wavelet Filter

In order to find the proper *scale* parameter for a given type of wavelet, the rise time of its dominant pulse has to be measured first. The time axis of a mother wavelet is always given in samples, so the measured rise time has to be multiplied by the sampling time of the used measuring equipment. This way the dimensionless *scale* parameter a_Ψ of the inspected Ψ mother wavelet is given by the ratio of the required and the measured rise time values, as shown in the following equation:

$$a_\Psi = \frac{T_{r,x}}{(T_s \cdot K_{r,\Psi})} \tag{5}$$

where $T_{r,x}$ (ns) is the rise time of the first pulse of the signal x, T_s (ns) is the sampling time of the used oscilloscope, and $K_{r,\Psi}$ (–) is the rise time of the dominant pulse of the mother wavelet Ψ in samples.

To consider the slight rise time deviations of the filtered pulses, a short interval of scale parameters was specified instead of an individual value. The lower and upper boundaries of this interval are given by the lowest 1.56 ns and the highest 1.70 ns values of the average results shown in Fig. 4.

The chosen wavelet families were the Daubechies (db), the Symlets (sym), and the Coiflets (coif), as these are the most commonly used in the literature [15], [16], [18], [20], [21]. In total, 22 wavelet types have been examined, namely the *db1–db10*, the *sym2–sym8,* and the *coif1–coif5* wavelets, as these are the most commonly used orders of these wavelet families.

For each wavelet function, the required interval of *scale* parameters was specified according to (5) before further examinations. The wavelet functions of the examined wavelet types are illustrated in Fig. 5.

B. Wavelet First Pulse Algorithm

The newly developed wavelet first pulse (WFP) algorithm utilizes the fact that when an emitted corona discharge pulse is measured, the first part of the signal is low energy noise, followed by the searched steep pulse and a slower oscillation with much higher energy content. Therefore, the two key operations of this algorithm are the calculation of the CWT and the so-called cumulative energy curve of the measured noisy signal. The CWT highlights the steep pulses of the signal, whereas the cumulative energy curve roughly shows the beginning of the high energy content signal, narrowing down the region where the first pulse is searched. With all this in mind, the steps of the WFP algorithm are described below and illustrated in Fig. 6 using one of the *ac-negative* signals with additive white Gaussian noise. The *original* and the *noisy* signals are shown in Fig. 6(a).

Step #1: The CWT $W_x(a, b)$ of the noisy signal $x(t)$ is calculated according to (4), using the chosen mother wavelet Ψ and its previously specified interval of the *scale* parameter a_Ψ.

Step #2: The 2-D wavelet coefficients of $W_x(a, b)$ are converted into the single time-domain signal $x_{cwt}(t)$ by averaging the results along the *scale* axis as follows:

$$x_{cwt}\left(t|_{t=b}\right) = \underset{a}{\text{avg}}\left\{W_x\left(a,b\right)\right\}. \tag{6}$$

Step #3: At each t_i time value where the polarity of $x(t_i)$ and $x_{cwt}(t_i)$ is reversed, the value of $x_{cwt}(t_i)$ is set to zero, as shown in (7). This step helps to exclude the false peaks of the filtered signal. The resulting time-domain signal is shown in Fig. 6(b)

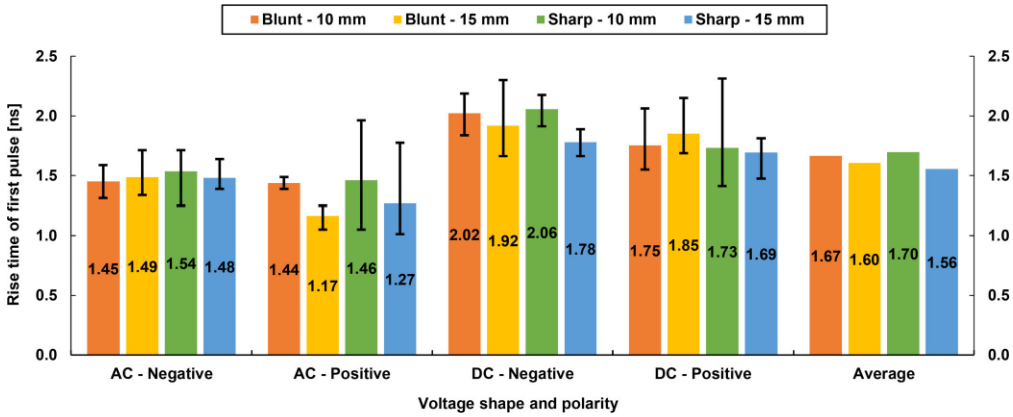

Fig. 4. Rise time of the first corona pulse for different voltage types and electrode arrangements.

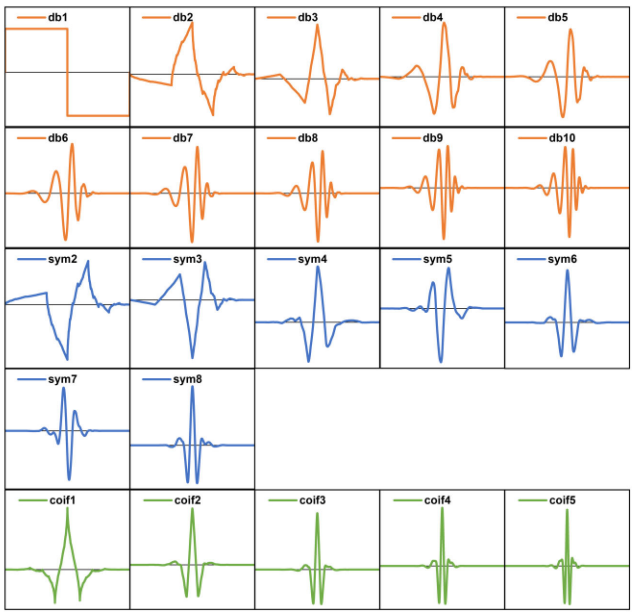

Fig. 5. Illustration of the examined 22 wavelet functions.

as *cwt*

$$\text{if}: x_{cwt}(t_i) = x(t_i), \text{ then: } x_{cwt}(t_i) := 0. \tag{7}$$

Step #4: The cumulative energy curve *S*(*t*) of the original signal *x*(*t*) is calculated according to (8), where *N* is the number of discrete data points in the sampled signal, and S_i is the cumulative energy of the signal at the *i*th time value t_i [22]. This curve first decreases from zero to its minimum value and starts to increase when the energy content of the signal becomes greater than the average value. This means that the curve reaches its minimum value roughly at the first peak of the corona signal

$$S(t_i) = S_i - i \cdot \frac{S_N}{N} \tag{8}$$

$$\left(S_i = \sum_{k=1}^{i} x(t_k)^2;\ i = 1,\ 2,\ 3,\ \ldots,\ N \right).$$

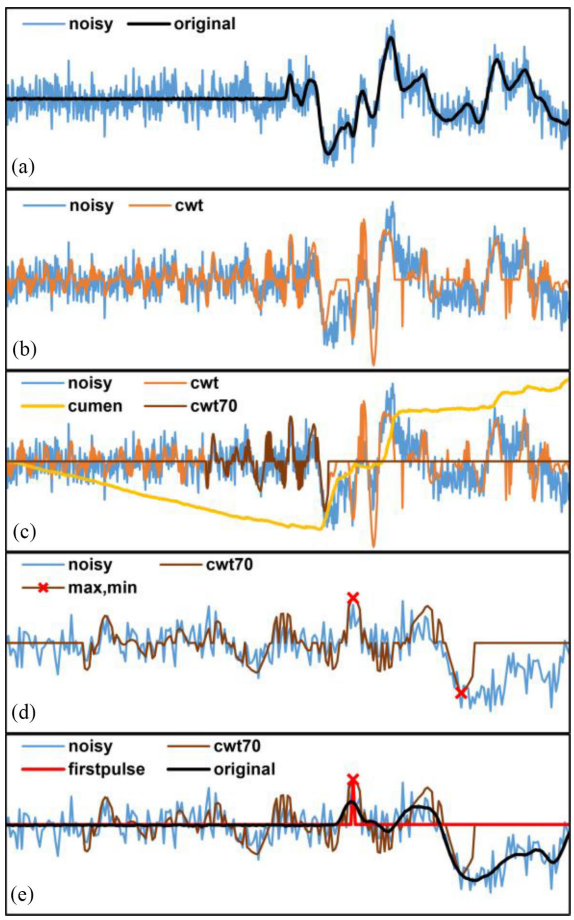

Fig. 6. The main steps of the developed WFP algorithm.

Step #5: At each t_i time value where *S*(t_i) is above 70% of its minimum value, the value of $x_{cwt}(t_i)$ is set to zero, as shown in (9). This step helps to focus the search near the beginning of the corona signal. The resulting time-domain signal is shown in Fig. 6(c) where *cwt70* along with the cumulative energy curve is shown as *cumen*

$$\text{if}: S(t_i) > 0.7 \cdot \min_t \{S(t)\}, \text{ then: } x_{cwt}(t_i) := 0. \tag{9}$$

Step #6 (modified in Fig. 10*):* The time instances of the minimum and maximum values of the modified x_{cwt} (*cwt70*) are calculated ($t_{\min}$, $t_{\max}$), and the final arrival time of the first pulse ($t_{\text{firstpulse}}$) is defined as the earlier of these two values, as describe in (10). This step makes the algorithm suitable for both positive and negative first pulses. The parts of this step are shown in Fig. 6(d) and (e) as max, min, and firstpulse

$$t_{\text{firstpulse}} = \min\{t_{\min}, t_{\max}\} \quad (10)$$
$$\left(\min_t\{x_{cwt}(t)\} = x_{cwt}(t_{\min});\right.$$
$$\left.\max_t\{x_{cwt}(t)\} = x_{cwt}(t_{\max})\right).$$

C. Examination Results

To compare the 22 examined wavelet types, the original 80 signals shown in Table II were doubled, and each copy was shifted by 20 ns to test the TDOA determination accuracy of the WFP algorithm. After this, randomly generated additive white Gaussian noise was added to the resulting 160 signals with signal-to-noise ratio (SNR) values ranging from 0 to 20 dBW in 2-dBW steps. This step was repeated 10 times, resulting in 800 different signal pairs for each SNR value. By doing so, for each original signal, we simulated that ten separate measurements were taken, whereas the original and the shifted signals came from the same discharge source having the same original waveform, but due to the physical environment and the two measuring antennas, different distortive noises were added to them. This means that for each one of the 22 wavelets, the WFP algorithm was tested on 17 600 different signals resulting in 8800 TDOA values.

For the first examination (#1), the absolute TDOA estimation errors were calculated and averaged for each wavelet type and SNR value separately. The resulting values were then normalized for each SNR value using the highest average absolute TDOA error of the 22 examined wavelets. This way, the resulting normalized values became independent from the SNR values, and by averaging them for each wavelet type, the results shown in Fig. 7 were given showing the resultant relative error of each wavelet type compared with the others.

The indicated normalized absolute errors in Fig. 7 are the averaged values, whereas the error bars show the highest and lowest individual values of the averaged 11 SNR results for each wavelet. The results show that *db*3, *sym*4, and *sym*5 provided the lowest errors regardless of the SNR value.

For the second examination (#2), the *db*3, *sym*4, and *sym*5 wavelets were chosen, and the simulations were repeated with an increased interval of SNR values ranging from -5 to 25 dBW in 1-dBW steps, and 20 separate noise additions for each signal, instead of the previous 10. The resulting absolute errors were averaged separately for each wavelet type, each SNR value, and each of the voltage type and polarity based four main arrangements shown in Table II. The resulting average values were then normalized for each SNR value using the average results of the three examined wavelets.

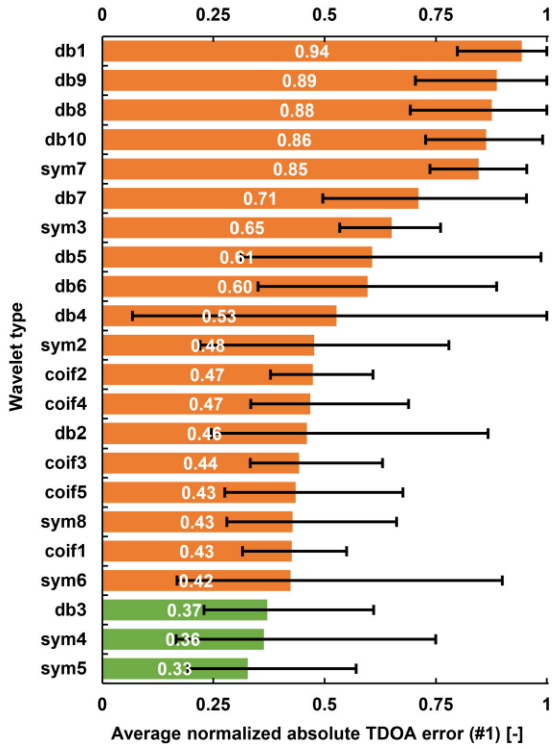

Fig. 7. Examination #1: average absolute TDOA errors of the 22 wavelets.

By averaging the normalized values for each wavelet and arrangement type, the results shown in Fig. 8 were given, where the indicated normalized absolute TDOA errors are the averaged values, whereas the error bars show the highest and lowest individual values of the averaged 31 SNR results for each wavelet and arrangement.

The average results shown in Fig. 8 show that generally there is no best wavelet; however, in the ac case the *db*3 wavelet whereas in the dc case the *sym*4 wavelet consistently provided better results. In most real-life cases, either by looking at the ac–dc waveform differences shown in Fig. 2 or by knowing the voltage type of the measured equipment, we can decide if the measured signals are ac or dc, so we can also choose the most suitable wavelet to be used.

With this in mind, for the third examination (#3), the *db*3 wavelet was chosen for ac cases, whereas for the dc measurements, the *sym*4 wavelet was used. By separating these two basic cases, the intervals of the *scale* parameters were also changed to better fit the rise time values of the ac and dc signals separately. The *scale* interval of the AC *db*3 wavelet was set to $a_{db3} = [14.5, 19.1]$, whereas for the DC *sym4* scales, it was set to $a_{sym4} = [16.0, 19.5]$. Equation (5) shows that in a general case, these values must be multiplied by F_s/4 GHz , if the sampling frequency is F_s.

Using these updated parameters, the TDOA values were calculated similarly to the second examination; however, this time the resulting errors were not the absolute values but the original signed ones. Fig. 9 shows the average value of the resulting *signed* TDOA errors of Examination #3 as a function

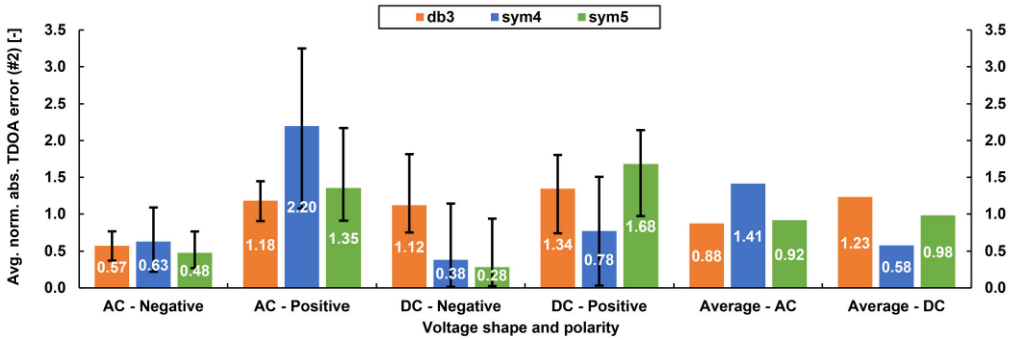

Fig. 8. Examination #2: average absolute TDOA errors of the chosen three wavelets for the ac and dc cases.

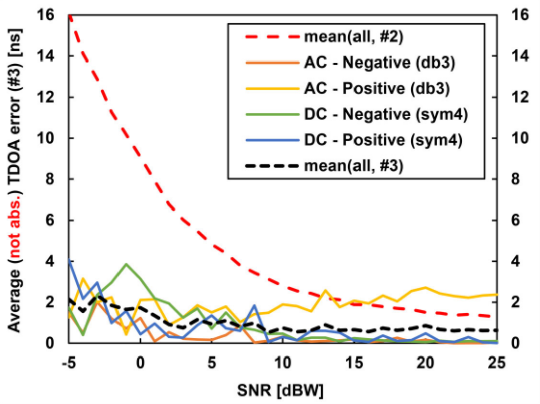

Fig. 9. Examination #3: average signed TDOA errors of the final wavelets.

of the SNR value compared with the average *absolute* value of Examination #2.

The results show that by averaging the measured TDOA values, most of their individual errors can be eliminated, providing accurate input TDOA parameters for the location approximation algorithms. However, the results shown in Figs. 8 and 9 also show that the errors of the *ac-positive* arrangement are much higher than the results of the other three. The reason to this phenomenon is that the ac signals start with two pulses of the same polarity, whereas in case of the dc signals, the first pulse is followed by an opposite polarity one, as the representative signals in Fig. 2 show.

In the case of the problematic *ac-positive* signals, this second pulse has a slightly higher amplitude, and therefore depending on the random nature of the noise, the WFP algorithm may choose both pulses as the first one. Because of their oscillating behavior, the wavelet functions also tend to highlight those consecutive pulse pairs that have opposite polarities.

With all this in mind, *Step* #6 of the WFP algorithm was modified to detect whether there is a significant pulse between the determined minimum and maximum values of x_{cwt} that has the same polarity as the first one. This intermediate pulse is then chosen as the output first pulse if its amplitude is at least 25% of the first determined one. Fig. 10 illustrates the accordingly *modified Step* #6 of the WFP algorithm.

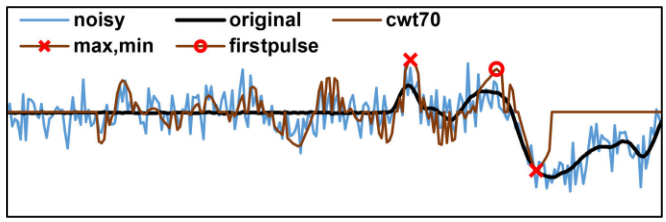

Fig. 10. The modified Step #6 of the WFP algorithm.

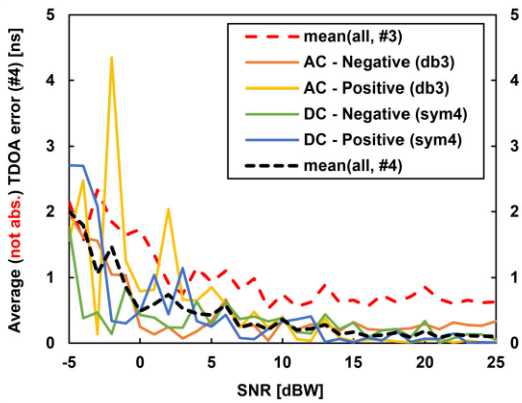

Fig. 11. Examination #4: average signed errors of the modified algorithm.

During the last examination (#4), the average signed TDOA errors were calculated similar to the third examination to test the accuracy of the modified WFP algorithm. Fig. 11 shows the average TDOA errors of Examination #4 as a function of the SNR value compared with the average errors of Examination #3. The results show that by using the modified WFP algorithm, the problematic *ac-positive* errors were eliminated, reducing the average errors significantly. It can also be seen that above the 5-dBW SNR value, the average errors become consistently negligible and stay well below 1 ns.

The final goal of this research is to create a corona discharge location approximation system; therefore, the primary question is the positioning accuracy that the TDOA values of the WFP algorithm can provide. To answer this question, Fig. 12 visualizes the distribution of the individual TDOA estimations and

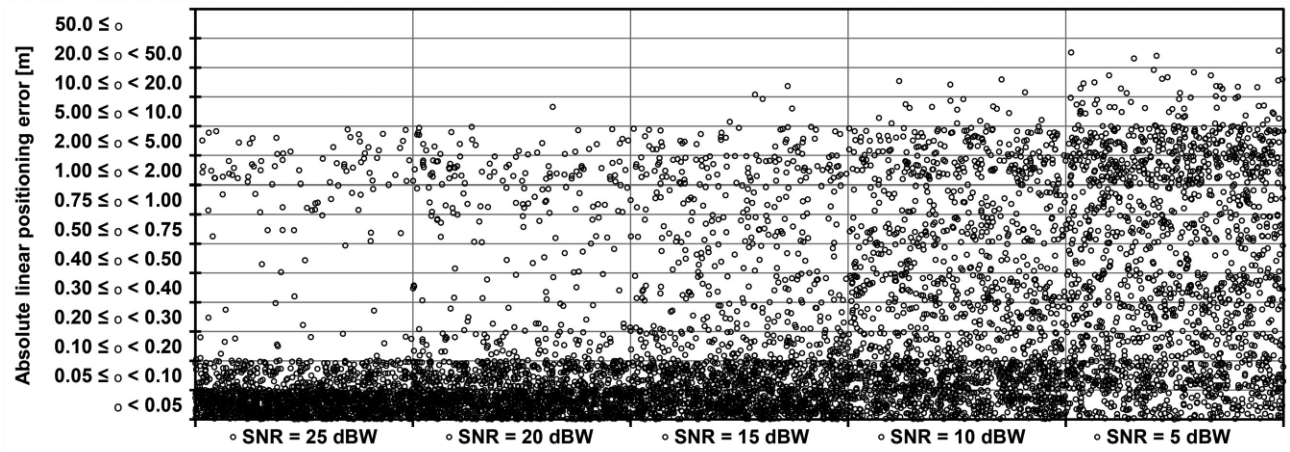

Fig. 12. Absolute linear positioning errors caused by the individual TDOA errors of the WFP algorithm.

their effect on the location approximation accuracy of a linear positioning problem, showing 1600 separate data points for each observed SNR value.

The distribution of individual positioning errors show that above the 5-dBW SNR value, most of the individual errors are below 10 cm. In an industrial or high-voltage environment, such accuracy is perfectly sufficient to find the faulty part of the inspected equipment. This accuracy is also achievable at lower SNR values (higher noise levels) by excluding those measurement results that highly deviate from the mean value of the data set. This way, only the accurate results will be kept, so their mean value will be even more accurate.

IV. Conclusion

The aim of the presented research was to obtain the needed parameters and create a novel algorithm for the noise filtering module of a corona discharge location approximation system that could be used in various fields of industry applications, where the presence of corona discharges is unwanted. To accurately measure the arrival times of the emitted electromagnetic signals of corona discharges, the WFP algorithm has been developed to highlight the first pulses of the captured signals in time domain. This algorithm is based on the CWT, and it considers the waveform of the observed discharge pulse.

Depending on the type of the observed corona discharge, two separate wavelet functions have been chosen, namely the order 3 Daubechie (*db*3) wavelet for ac cases and the order 4 Symlet (*sym*4) wavelet for dc measurements. The *scale* parameters of these wavelets have been set to the intervals of $a_{db3} = [14.5, 19.1]$ and $a_{sym4} = [16.0, 19.5]$ to properly match the measured rise time values of the emitted ac and dc corona signals. In a general case, with a sampling frequency of F_s, these *scale* values must be multiplied by the dimensionless multiplier of F_s/4 GHz.

By modifying *Step* #6 of the WFP algorithm, instead of finding the first single pulse, the first polarity changing pair of pulses is highlighted in the filtered signal. This makes the ac measurements much more reliable, by eliminating the uncertainty caused by their two similar starting pulses.

The final version of this algorithm provides TDOA values accurate enough to reduce the location approximation error to a few centimeters, making it perfect for industrial applications.

As a next step, the effect of different antenna types on the waveform and rise time of the corona pulse must also be investigated for the final applicability of the positioning system. Also, a similar examination must be performed on the emitted signals of void and surface discharges [23], because of their significance in various malfunctions of high-voltage equipment [24]–[27]. The polarity changing oscillation focused approach of the final WFP algorithm can also be utilized for the emitted waveforms of these discharges because they all show similar oscillating behavior [28]–[30]. The final objective of our broader research is to create a PD positioning system that could be generally applied for all kinds of partial discharges in various industry applications.

References

[1] S. A. Mahmood Najafi, A. Peimankar, H. Saadati, E. Gockenbach, and H. Borsi, "The influence of corona near to the bushing of a transformer on partial discharge measurement with an acoustic emission sensor," in *Proc. IEEE Elect. Insul. Conf.*, Ottawa, ON, USA, 2013, pp. 295–298.

[2] G. Mitic and G. Lefranc, "Localization of electrical-insulation and partial-discharge failures of IGBT modules," *IEEE Trans. Ind. Appl.*, vol. 38, no. 1, pp. 175–180, Jan./Feb. 2002.

[3] M. Liu, J. Tang, Q. Yao, and Y. Miao, "Development processes of positive and negative DC corona under needle-plate electrode in air," in *Proc. IEEE Int. Conf. High Voltage Eng. Appl.*, Chengdu, China, 2016, pp. 1–4.

[4] M. Au, B. L. Agba and F. Gagnon, "A model of electromagnetic interferences induced by corona discharges for wireless channels in substation environments," *IEEE Trans. Electromagn. Compat.*, vol. 57, no. 3, pp. 522–531, Jun. 2015.

[5] D. Moongilan, "Corona noise considerations for smart grid wireless communication and control network planning," in *Proc. IEEE Int. Symp. Electromagn. Compat.*, Pittsburgh, PA, USA, 2012, pp. 357–362.

[6] B. G. Stewart, A. Nesbitt, and L. Hall, "Triangulation and 3D location estimation of RFI and partial discharge sources within a 400 kV substation," in *Proc. IEEE Elect. Insul. Conf.*, Montreal, QC, Canada, 2009, pp. 164–168.

[7] J. M. Fresno, G. Robles, J. M. Martínez-Tarifa and B. G. Stewart, "A combined algorithm approach for PD location estimation using RF antennas," in *Proc. IEEE Elect. Insul. Conf.*, Baltimore, MD, USA, 2017, pp. 384–387.

[8] O. El Mountassir, B. G. Stewart, A. J. Reid, and S. G. McMeekin, "Quantification of the performance of iterative and non-iterative computational methods of locating partial discharges using RF measurement techniques," *Elect. Power Syst. Res.*, vol. 143, pp. 110–120, 2017.

[9] J. Petráš, J. Džmura, and M. Kosterec, "Partial discharge signal de-noising by morphological filters," in *Proc. 19th Int. Sci. Conf. Elect. Power Eng.*, Brno, Czech Republic, 2018, pp. 1–5.

[10] K. Firuzi and M. Vakilian, "Multi-source partial discharge signals discrimination by six bandpass filters and DBSCAN clustering," in *Proc. 12th Int. Conf. Properties Appl. Dielect. Mater.*, Xi'an, China, 2018, pp. 68–71.

[11] C. Abadie, T. Billard, and T. Lebey, "Partial discharges in motor fed by inverter: From detection to winding configuration," *IEEE Trans. Ind. Appl.*, vol. 55, no. 2, pp. 1332–1341, Mar./Apr. 2019.

[12] M. Szirtes and R. Cselkó, "Simulation of corona discharges and time domain examination of their emitted electromagnetic signals," in *Proc. 7th Int. Youth Conf. Energy*, Bled, Slovenia, 2019, pp. 1–5.

[13] M. Szirtes, R. Cselkó, and I. Berta, "Examination of the emitted electromagnetic signals of corona discharges," in *Proc. IEEE Ind. Appl. Soc. Annu. Meeting*, Baltimore, MD, USA, 2019, pp. 1–5.

[14] Xiaodi Song, M. Judd, and C. Zhou, "An optimal algorithm for applying wavelet transform in identifying the arrival time of PD pulse in a UHF detection system," in *Proc. 42nd Int. Universities Power Eng. Conf.*, Brighton, U.K., 2007, pp. 495–498.

[15] B. Raghavendra and M. K. Chaitanya, "Comparative analysis and optimal wavelet selection of partial discharge de-noising methods in gas-insulated Substation," in *Proc. 3rd Int. Conf. Adv. Elect., Electron., Inf., Commun. Bio-Inform.*, Chennai, India, 2017, pp. 1–5.

[16] A. Zaeni, T. Kasnalestari, and U. Khayam, "Application of wavelet transformation Symlet type and Coiflet type for partial discharge signals denoising," in *Proc. 5th Int. Conf. Elect. Veh. Technol.*, Surakarta, Indonesia, 2018, pp. 78–82.

[17] Y. Lu, X. Tan, and X. Hu, "PD detection and localisation by acoustic measurements in an oil-filled transformer," *IEE Proc. - Sci., Meas. Technol.*, vol. 147, no. 2, pp. 81–85, Mar. 2000.

[18] H. A. Vidya, V. Krishnan, and K. Mallikarjunappa, "A wavelet transform technique for de-noising partial discharge signals," in *Proc. Int. Conf. Condition Monit. Diagnosis*, Beijing, China, 2008, pp. 1104–1107.

[19] "XYZ's of Oscilloscopes," Tektronix, 01/16 EA 03W-8605-7, 2016, pp. 37–38.

[20] D. ZhaoHeng, L. ShangHe, and W. Lei, "Selection of the optimal wavelet bases for wavelet de-noising of partial discharge signal," in *Proc. 2nd Int. Conf. Signal Process. Syst.*, Dalian, China, 2010, pp. V3-400–V3-404.

[21] P. Ray, A. Basuray and A. K. Maitra, "Optimum wavelet bases selection for wavelet based de-noising in partial discharge measurement," in *Proc. IEEE Conf. Inf. Commun. Technol.*, Thuckalay, India, 2013, pp. 1110–1113.

[22] O. El Mountassir, B. G. Stewart, S. G. McMeekin, and A. Ahmadinia, "Effect of noise on the location accuracy of partial discharges using radiated RF detection techniques," in *Proc. 47th Int. Universities Power Eng. Conf.*, London, U.K., 2012, pp. 1–6.

[23] M. Szirtes and R. Cselkó, "Simulation of void discharges and time domain examination of their emitted electromagnetic signals," in *Proc. 21st Int. Symp. High Voltage Eng.*, Budapest, Hungary, 2019, pp. 1–10.

[24] L. A. Renforth, R. Giussani, M. T. Mendiola, and L. Dodd, "Online partial discharge insulation condition monitoring of complete high-voltage networks," *IEEE Trans. Ind. Appl.*, vol. 55, no. 1, pp. 1021–1029, Jan./Feb. 2019.

[25] C. Malliou, A. D. Karlis, M. G. Danikas, and B. Lloyd, "A short review on the offshore wind turbine generator windings' insulation and the effect of water droplets and salinity," *IEEE Trans. Ind. Appl.*, vol. 52, no. 6, pp. 4610–4618, Nov./Dec. 2016.

[26] L. A. Renforth, P. S. Hamer, D. Clark, S. Goodfellow, and R. Tower, "Continuous remote online partial discharge monitoring of HV Ex/ATEX motors in the oil and gas industry," *IEEE Trans. Ind. Appl.*, vol. 51, no. 2, pp. 1326–1332, Mar./Apr. 2015.

[27] G. C. Stone, H. G. Sedding, and C. Chan, "Experience with online partial-discharge measurement in high-voltage inverter-fed motors," *IEEE Trans. Ind. Appl.*, vol. 54, no. 1, pp. 866–872, Jan./Feb. 2018.

[28] R. Bartnikas, "Partial discharges. Their mechanism, detection and measurement," *IEEE Trans. Dielect. Elect. Insul.*, vol. 9, no. 5, pp. 763–808, Oct. 2002.

[29] R. Sarathi, I. P. Merin Sheema, and J. S. Rajan, "Understanding surface discharge activity in copper sulphide diffused oil impregnated pressboard under AC voltages," *IEEE Trans. Dielect. Elect. Insul.*, vol. 21, no. 2, pp. 674–682, Apr. 2014.

[30] J. A. Kay, G. A. Hussain, M. Lehtonen, and L. Kumpulainen, "New preemptive arc-fault detection techniques in medium-voltage switchgear and motor controls," *IEEE Trans. Ind. Appl.*, vol. 52, no. 1, pp. 740–750, Jan/Feb. 2016.